



Cite this: *RSC Adv.*, 2024, 14, 9968

# Role of iron oxide in retarding the graphitization of de-oiled asphaltenes for amorphous carbon

Zhiwei Liu,  Ning Pu, Yanxia Yuan, Qinghe Yang, Haiping Shen, Hong Nie,\*  
Ranran Hou and Chuangchuang Yang

The solvent deasphalting (SDA) process is widely recognized as a significant technology in processing inferior oil. However, de-oiled asphaltene (DOA), which accounts for about 30% of feedstocks, is not well utilized in conventional processing methods to date. Considering its complicated structure and high heteroatom and metal contents, DOA is suitable for preparing amorphous carbon. Herein, we obtained amorphous carbon from inferior de-oiled asphaltene through direct carbonization of a mixture of DOA and  $\text{Fe}_2\text{O}_3$  and revealed the mechanism of iron oxide in retarding graphitization to increase the disordered structure content. After the addition of  $\text{Fe}_2\text{O}_3$ , XRD results showed that the content of amorphous carbon increased from 25.57% to 59.48%, and a higher defect degree could also be observed in Raman spectra, thus resulting in better electrochemical performance in Na-ion half-cells. As a coke core,  $\text{Fe}_2\text{O}_3$  could accelerate the polycondensation of asphaltene molecules; meanwhile, oxygen species derived from  $\text{Fe}_2\text{O}_3$  could capture excess H free radicals in the initial pyrolysis stage, which inhibited the formation of planar polycyclic aromatic molecules and weakened  $\pi$ - $\pi$  interactions. Moreover, O atoms could embed into the carbon skeleton by reacting with DOA at higher temperatures, which could further twist and break the intact carbon layer. Both of the factors enhanced the proportion of amorphous carbon. This work not only provides a new understanding of controlling the carbonization process, but it also promotes the development of the SDA process.

Received 25th January 2024  
Accepted 11th March 2024

DOI: 10.1039/d4ra00642a

rsc.li/rsc-advances

## Introduction

During the last decades, there has been growing concern about environmental problems and the declining trend of heavy oil quality.<sup>1,2</sup> Highly efficient utilization of heavy oil has become a serious challenge. Asphaltenes, the most complicated and polar fractions, bring about a series of problems in the processing of inferior heavy oil.<sup>3,4</sup> Solvent deasphalting (SDA) is widely considered an economic and important method to decrease the asphaltene content in inferior oil.<sup>5</sup> SDA technology separates inferior oils into deasphalted oil (DAO) and de-oiled asphaltene (DOA) using paraffinic solvents. DAO is a higher-quality feedstock for hydrotreating and fluid catalyst cracking; however, DOA, accounting for a considerable amount (about 30%) of feedstock, is difficult to be utilized by conventional processing methods.<sup>6</sup>

As the heaviest fraction in the SDA process, DOA contains high heteroatom (S, N, O) and metal (Ni, V, *etc.*) contents, high polarity, high molecular weight, and the most complicated structure.<sup>7</sup> Due to high reactivity, DOA tends to form coke in conventional decarbonization and hydrogenation.<sup>8</sup> Carbon and metal deposition caused by DOA lead to the rapid deactivation

of a catalyst and short run time in the refining process.<sup>9,10</sup> Therefore, DOA can be only applied in road asphalt or mixed with fluid catalytic cracking (FCC) slurry oil to produce inferior coke. It severely restricts the efficient utilization of heavy oil and the development of solvent deasphalting processing.

Moreover, with the rapid development of renewable energy sources, electrochemical energy storage devices play a crucial role in the utilization of clean energy by providing storage support for various electronics.<sup>11,12</sup> Benefiting from the abundant resources, lower cost, and wide distribution of Na, sodium ion batteries (SIBs) have recently attracted considerable attention as the next-generation storage technology.<sup>13–18</sup> Although sodium possesses similar physicochemical properties as lithium,<sup>19</sup> graphite cannot form a stable Na–C compound due to thermodynamic factors<sup>20</sup> and shows poor Na storage capacity. Nowadays, the main challenge faced by SIBs is the development of anode materials.<sup>21</sup> Undoubtedly, carbonaceous anodes are one of the most promising materials for SIBs from the aspect of practical application.<sup>22</sup>

Considering the high carbon content and low cost, DOA is a potential raw material for synthesizing carbon materials. Amorphous carbon holds lots of defects, has an inherent larger interlayer distance, and is considered a suitable material for SIBs anodes.<sup>23</sup> However, due to the higher H content and stronger  $\pi$ - $\pi$  interactions between planar aromatic molecules,

Research Institute of Petroleum Processing, SINOPEC, Beijing, 100083, PR China.  
E-mail: niehong.ripp@sinopec.com



the materials obtained by the pyrolysis of pitch exhibit a higher graphitization degree, which is detrimental to the storage of sodium ions.<sup>24,25</sup> In order to solve this problem, there is a growing body of literature on modification strategies for pitch-based carbon materials.<sup>26,27</sup> Wei *et al.* obtained N-doped porous carbon nanosheets (NPCS) using a NaCl/KCl mixture as a template after heat treatment under NH<sub>3</sub>/Ar mixed gas. NPCS could deliver a high reversible capacity of 313.6 mA h g<sup>-1</sup> at 0.1 A g<sup>-1</sup> for SIBs.<sup>28</sup> Daher *et al.* prepared hard carbon through per-oxidation at 300 °C for 12 h followed by carbonization at 1400 °C for 2 h; such material could exhibit 312 mA h g<sup>-1</sup> reversible capacity at C/20 and higher initial coulombic efficiency (ICE) of 90% for SIBs.<sup>29</sup> Generally, the pitch used in most of the works was high-quality commercial asphalt. In fact, it is the use of inferior DOA that determines the economic benefit and the development of solvent deasphalting processing in the industry, but the corresponding reports are few because of the terrible quality of DOA, *i.e.* higher metal content and the complicated ingredient. Moreover, most studies in the field of SIBs have only focused on the relationship between electrochemical performance and carbon materials. Previous studies have not dealt with the regulatory mechanism for converting pitch to amorphous carbon.

Herein, we propose a simple strategy to retard the graphitization of DOA and prepare highly disordered amorphous carbon by mixing it with Fe<sub>2</sub>O<sub>3</sub>. Moreover, based on the results of TG-MS and XPS, this study elucidated the mechanism of iron oxide in retarding graphitization to increase disordered structures. It was found that Fe<sub>2</sub>O<sub>3</sub> could take away excessive hydrogen in the initial stage of pyrolysis, which suppressed the melting and reordering of pitch. With the increase in temperature, C and S species of DOA could be oxidized by Fe<sub>2</sub>O<sub>3</sub>, which further twisted carbon layers and increased the amorphous degree. Finally, this highly disordered amorphous carbon exhibited a higher Na storage capacity than the sample without Fe<sub>2</sub>O<sub>3</sub>. This work will promote the development of solvent deasphalting processing and provide new insights into heavy oil processing.

## Experimental

### Synthesis of materials

The de-oiled asphaltene was supplied by the Sinopec Group and obtained from the industrial unit of Solvent Deasphalting Processing. The main properties of the DOA are listed in Table 1. The de-oiled asphaltene and other chemicals were used as received without further treatment. The preparation of the sample was performed with reference to the literature<sup>30</sup> with some modifications. In order to evenly mix the DOA and iron, 2.0 g DOA was dissolved in 60 mL toluene under sonication dispersion for 20 min, and 8.0 g Fe<sub>2</sub>O<sub>3</sub> with particle sizes of about 50 nm was added into the solution under stirring. Toluene was removed by distillation at 160 °C in an oil bath after stirring for 30 min. To ensure that DOA can be more evenly coated on the iron oxide, the prepared homogeneous mixture was firstly pre-oxidized at 300 °C for 3 h under air and then calcined at 800 °C for 2 h under the N<sub>2</sub> atmosphere. The heating

Table 1 Properties of DOA

Items	Value
Carbon residue (wt%)	48.4
<b>Elemental composition (wt%)</b>	
C	83.31
H	8.12
S	7.52
N	0.42
<b>Group analysis (wt%)</b>	
Saturates	0
Aromatics	16.1
Resins	27.6
Asphaltenes	56.3
<b>Metal content (μg g<sup>-1</sup>)</b>	
Ni	91.3
V	281
Fe	96.4
Na	32.9
Ca	7.8

rate was 5 °C min<sup>-1</sup>. Fe<sub>2</sub>O<sub>3</sub> was removed by using 3 M HCl at 80 °C under stirring. The sample (named DO) was collected by suction filtration for 30 min with deionized water, centrifuged 5 times, and dried at 80 °C for 3 h. The element analysis showed that the Fe content is about 0.01%. As a comparison, the DOA was calcined at 800 °C for 2 h under the N<sub>2</sub> atmosphere to obtain material D.

### Characterization of materials

The morphology was investigated using field emission scanning electron microscopy (SEM, Hitachi SU-8010) and high-resolution transmission electron microscopy (HRTEM, Philips Tecnai G2 F20). The content of elements was obtained by a Vario EL III elemental analyzer (Elementar, Germany). The crystalline structure was characterized by X-ray powder diffraction (XRD, Bruker D5005 X'Pert) with Cu Kα radiation, and XRD patterns were collected from 2θ = 5° to 2θ = 70° at a scan rate of 2° min<sup>-1</sup>. N<sub>2</sub> adsorption-desorption was used to examine the specific surface area and pore structure using a Micromeritics ASAP 2002 analyzer. Raman experiment was carried out on a Raman spectrometer (LabRAM HR UV-NIR, Jobin Yvon) using a 532 nm line (Nd-YAG laser). X-ray photoelectron spectroscopy (XPS) was performed on a VG scientific ESCA Lab 250 spectrometer with AlKα radiation and the obtained data were fitted by Advantage. Infrared spectroscopy (IR) was performed on a Thermo Fisher Scientific spectrometer. Thermogravimetry mass spectrometry (TG-MS) was analysed on a NETZSCH STA409PC-QMS403 instrument from 50 to 800 °C at 5 °C min<sup>-1</sup>.

### Electrochemical measurements

The working electrode was prepared by mixing 90 wt% active materials, 5 wt% styrene butadiene rubber (SBR) and 5 wt% carboxymethyl cellulose (CMC) in deionized water to form a uniform slurry. The slurry was coated on a Cu foil and dried at



110 °C overnight under vacuum. Then, the coated copper foil was fabricated into CR2032 button cells using pure Na foil as the counter electrode. The assembly of the battery was performed in an argon-filled glove box ( $\text{H}_2\text{O} < 0.01$  ppm,  $\text{O}_2 < 1$  ppm). The electrolyte was 1 M  $\text{NaPF}_6$  dissolved in diethylene glycol dimethyl ether (diglyme), and the glass fiber was used as a separator. The galvanostatic charge/discharge tests were performed on a Land CT2001A battery test system (Wuhan, China) with a potential window of 0.005–3.0 V at room temperature.

## Results

### Structural features of materials

The effects of  $\text{Fe}_2\text{O}_3$  on the morphology and the crosslinking mode have been investigated using the SEM and TEM images displayed in Fig. 1. The SEM image of D (Fig. 1a) shows a smooth surface, while DO exhibits a coarse and shaggy surface (Fig. 1b), indicating that  $\text{Fe}_2\text{O}_3$  acted as a coke core and asphalt molecules condensed around  $\text{Fe}_2\text{O}_3$ . Moreover, it could be observed in the lower magnification TEM results that D shows a relatively compact structure (Fig. 1c), while DO displays a pore structure (Fig. 1d), which further confirms that  $\text{Fe}_2\text{O}_3$  is the core in the condensation of DOA. For more details about the

microstructure, HRTEM was used to investigate the structural features of the two samples, and the results are illustrated in Fig. 1e and f. As shown in Fig. 1e, sample D exhibits longer and orderly graphite crystallites; in contrast, DO possessed shorter and twisty stripe structures, indicating that DO contains more amorphous carbon. During the thermal treatment process, the planar polycyclic aromatic molecules (PPAM) were formed through the pyrolysis, aromatization and polycondensation of asphalt molecules. The PPAMs show stronger  $\pi$ – $\pi$  interactions, which could promote the formation of an ordered graphite structure in sample D.<sup>24,31</sup> After the addition of  $\text{Fe}_2\text{O}_3$ , asphalt molecules could react with  $\text{Fe}_2\text{O}_3$ , which hindered the formation of PPAMs and impeded the  $\pi$ – $\pi$  interactions, and as a result, DO possessed a more disordered structure.

XRD analysis and Raman spectroscopy were further applied to investigate the microstructure of the two samples. As illustrated in Fig. 2a, both samples exhibit two diffraction peaks at around  $2\theta = 24^\circ$  and  $43^\circ$ , which could represent respectively the (002) and (100) crystallographic planes of low graphitized carbon,<sup>32,33</sup> indicating the formation of an amorphous structure. Compared with D, the (002) diffraction peak of DO shifts to a lower angle, demonstrating that DO could exhibit a larger interlayer spacing. Meanwhile, it could also be seen that DO

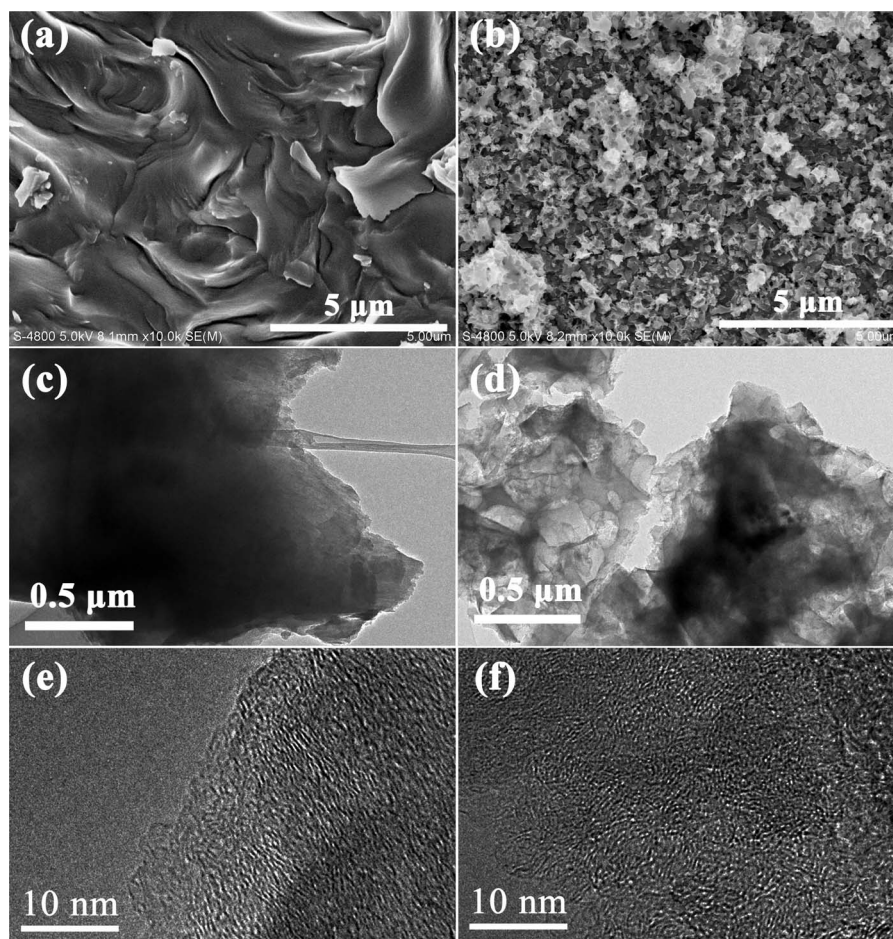


Fig. 1 SEM images of D (a) and DO (b); TEM and HRTEM images of D (c and e) and DO (d and f).





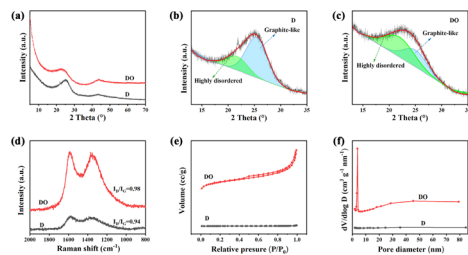


Fig. 2 XRD patterns (a), peak fitting of the (002) peaks of D (b) and DO (c), Raman spectra (d), N<sub>2</sub> physisorption isotherms (e) and pore size distributions (f) of the synthesized materials.

shows a wider and weaker (002) peak than D, indicating that the addition of Fe<sub>2</sub>O<sub>3</sub> could decrease the crystallite size and/or increase the defect degree. In order to identify the effect of Fe<sub>2</sub>O<sub>3</sub> on the microcrystalline structure, the (002) peaks were simulated by a profile-fitting process based on the literature<sup>34</sup> and the results are displayed in Fig. 2b and c and Table 2. Generally, the peak located around 22° is assigned to highly disordered amorphous carbon, which has a d-spacing larger than 0.4 nm and this structure is beneficial for the Na<sup>+</sup> transformation.<sup>27,35</sup> The peaks located at around 25° are attributed to a well-organized graphite-like phase. According to Fig. 2b and c and Table 2, sample D possesses only 25.57% amorphous carbon, but the carbon material DO shows 59.84% after the addition of Fe<sub>2</sub>O<sub>3</sub>, which is consistent with the HRTEM result. The structural evolution caused by Fe<sub>2</sub>O<sub>3</sub> could also be confirmed by the Raman spectra in Fig. 2d. It is widely considered that the D band at 1340 cm<sup>-1</sup> is assigned to the disordered carbon structure caused by sp<sup>3</sup>-hybrid carbon, and the G band (the in-plane vibrational mode) located at 1590 cm<sup>-1</sup> belongs to the regular graphitic structure caused by strong π-π interactions.<sup>36,37</sup> After the addition of Fe<sub>2</sub>O<sub>3</sub>, the intensity ratio I<sub>D</sub>/I<sub>G</sub> of DO (0.98) is higher than D (0.94), indicating that Fe<sub>2</sub>O<sub>3</sub> inhibits the formation of the graphitic structure and increases the disorder degree. The N<sub>2</sub> adsorption-desorption was used to evaluate the texture difference between the two samples. As displayed in Fig. 2e, the sample DO shows a type IV isotherm with a hysteresis loop, suggesting a mesoporous structure.<sup>38</sup> Fig. 2f displays that the pore size of DO focuses on 5 nm. At the same time, the BET surface area and pore volume of DO are larger than those of D (460 vs. 1.54 m<sup>2</sup> g<sup>-1</sup> and 0.38 vs. 0.0039 mL g<sup>-1</sup>, respectively). The results of N<sub>2</sub> adsorption-

desorption further proved that the asphalt molecules polycondensed with Fe<sub>2</sub>O<sub>3</sub> as the core, which is also consistent with the HRTEM result.

In order to elucidate the role of Fe<sub>2</sub>O<sub>3</sub> in the DOA high-temperature pyrolysis process, the TG-MS analysis of DOA and a mixture of DOA and Fe<sub>2</sub>O<sub>3</sub> are performed and the corresponding results are illustrated in Fig. 3. It can be seen that the pyrolysis performance of D is different from DO in the TG curves, indicating that there exist some chemical reactions between DOA and Fe<sub>2</sub>O<sub>3</sub> rather than just physical mixing. As shown in Fig. 3a, the TGA-curve of DOA exhibits a sharp weight loss between 400–500 °C, which could be attributed to the release of lots of volatile organic components caused by the pyrolysis, aromatization and polycondensation of asphalt molecules during the carbonization process.<sup>39</sup> The MS results (Fig. 3c–f) also show that a large amount of H<sub>2</sub>O and CO<sub>2</sub> could be detected at this stage, and some S atoms could be released as SO<sub>2</sub> due to the cleavage of the branched chain. After 700 °C, signals of CO<sub>2</sub> and SO<sub>2</sub> still could be observed, which could be attributed to the continuous polymerization of the planar polycyclic aromatic molecules and the further removal of heteroatoms, finally leading to the carbon microcrystal becoming more ordered and regular. After the addition of Fe<sub>2</sub>O<sub>3</sub>, the weight loss of the mixture could be divided into three stages in Fig. 3b: (1) 50–400 °C, the weight loss could be ascribed to the physical and chemical adsorption of water and volatile organic compounds. It can be found that the OH and H<sub>2</sub>O peaks of the mixture of DOA and Fe<sub>2</sub>O<sub>3</sub> are located at lower temperatures than DOA in Fig. 3c and d, indicating that Fe<sub>2</sub>O<sub>3</sub> can promote the pyrolysis of asphalt molecules and the content of H could be reduced through reaction with Fe<sub>2</sub>O<sub>3</sub>. According to Qi,<sup>25</sup> excessive hydrogen brings about the formation of a fusion state in the carbonization process; asphalt molecules have enough time to rearrange and generate PPAMs with strong π-π interactions, which is disadvantageous for obtaining an amorphous structure. Fe<sub>2</sub>O<sub>3</sub> could help take away lots of hydrogen and generate cross-linkages with asphalt molecules, which not only converts the fusion-state to solid-state carbonization, but also disrupts the π-π interactions, resulting in higher disorder degree. (2) 400–700 °C, an obvious weight loss can be found in Fig. 3b, which is caused by the pyrolysis, aromatization and polycondensation of asphalt molecules. CO<sub>2</sub>-MS curves show that the peak intensity of the mixture is higher than DOA, suggesting that Fe<sub>2</sub>O<sub>3</sub> acts as a coke core,

Table 2 Physical properties of DOA and the prepared materials

Sample	Element analysis (normalization)			XRD analysis		Texture properties	
	C, %	O, %	S, %	A <sub>d</sub> <sup>a</sup> , %	A <sub>g</sub> <sup>b</sup> , %	S <sub>g</sub> <sup>c</sup> , m <sup>2</sup> g <sup>-1</sup>	V <sub>p</sub> <sup>d</sup> , mL g <sup>-1</sup>
DOA	91.76	0.64	7.60	—	—	—	—
D	89.69	1.03	9.28	25.57	74.43	1.54	0.0039
DO	91.23	6.03	2.74	59.48	40.52	460	0.38

<sup>a</sup> The area of high disordered carbon. <sup>b</sup> The area of graphite-like. <sup>c</sup> BET surface area. <sup>d</sup> Pore volume.

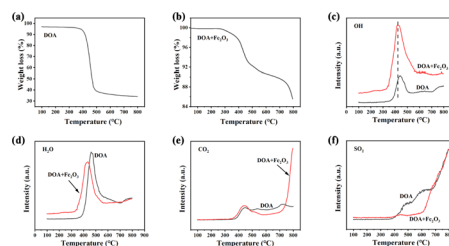


Fig. 3 TGA curves of DOA (a); TGA curves of the mixture of DOA and Fe<sub>2</sub>O<sub>3</sub> (b); the OH-MS (c), H<sub>2</sub>O-MS (d), CO<sub>2</sub>-MS (e) and SO<sub>2</sub>-MS (f) curve of two samples.

accelerating the pyrolysis and polycondensation reactions. (3) 700–800 °C, it is worth noting that a sharp weight loss could be observed in a mixture of DOA and  $\text{Fe}_2\text{O}_3$  but not in the DOA, and the corresponding MS result manifests the generation of lots of  $\text{CO}_2$ . With the temperature increasing over 700 °C, the carbon microcrystalline took part in the redox reaction with  $\text{Fe}_2\text{O}_3$ , and O atoms could be embedded into the skeleton to warp and destroy the carbon microcrystalline structure, thus increasing the layer spacing and defects. In addition,  $\text{SO}_2$ -MS curves (Fig. 3f) display that the  $\text{SO}_2$ -signal of the mixture is lower than that of DOA, indicating that S atoms preferentially react with  $\text{Fe}_2\text{O}_3$  to form  $\text{SO}_4^{2-}$  (as confirmed by the next XPS results) rather than decomposing to form  $\text{SO}_2$ . Moreover, combined with the results of the element analysis listed in Table 2, it could be reasonably inferred that  $\text{Fe}_2\text{O}_3$  also increases the removal of S atoms, further resulting in the distortion and deformation of carbon layers.

FT-IR was applied to analyse the change in functional groups on the surface after the addition of  $\text{Fe}_2\text{O}_3$ , and the results are illustrated in Fig. 4a. The broad bands around 2920 and 2850  $\text{cm}^{-1}$  were attributed to the stretching vibration of C–H, which is contributed by  $-\text{CH}_2-$ .<sup>40</sup> The intensity of  $-\text{CH}_2-$  becomes weaker after the introduction of iron oxide, indicating that  $\text{Fe}_2\text{O}_3$  could assist in removing the excess H atoms and promoting the thermal polymerization of DOA. The peaks around 1260 and 1100  $\text{cm}^{-1}$  were assigned to the C–O–C of aromatic ether groups (Ar–O–Ar) and aliphatic ether groups (R–O–C), respectively.<sup>41,42</sup> It could clearly be seen that the peak around 1100–1300  $\text{cm}^{-1}$  of DO is stronger than that of D, demonstrating that O atoms in  $\text{Fe}_2\text{O}_3$  successfully entered into the carbon skeleton in the form of C–O–C through a redox reaction with asphalt molecules.

Consistent with the TG-MS and FTIR results mentioned above, the surface element statuses obtained by XPS also demonstrated a potential chemical interaction between DOA and  $\text{Fe}_2\text{O}_3$ . As shown in Fig. 4b, the C 1s, O 1s, S 2s and S 2p could be detected in both samples, indicating that the O and S were the main heteroatoms after carbonization. Furthermore, in order to study the chemical bond configuration in detail, the

**Table 3** The relative content of C 1s, O 1s and S 2p peaks in deconvoluted samples

	C 1s (%)			O 1s (%)		S 2p (%)	
Sample	C=C	C-O	C=O	C-O	-COOH	C-S-C	SO <sub>4</sub> <sup>2-</sup>
D	80.63	16.49	2.88	71.47	28.53	94.36	5.64
DO	66.90	22.99	10.11	64.20	35.80	81.84	18.16

high-resolution XPS spectra of C 1s, O 1s and S 2p are depicted in Fig. 4c–h, and the corresponding deconvolution results are listed in Table 3. Generally, the C 1s could be divided into three carbon environments, which are C–C (284.6 eV), C–O (285.8 eV) and C=O (289.3 eV),<sup>43,44</sup> respectively. As for O 1s, the peak at 532.1 eV belonged to C–O and the band at 533.3 eV was associated with –COOH.<sup>31</sup> The S elements in the materials possess two states; the peaks at S 2p<sub>3/2</sub> (163.7 eV) and S 2p<sub>1/2</sub> (165 eV) were associated with –C–S–C– in thiophene, thioether and/or disulfide,<sup>45</sup> and the band located at 168.90 eV was attributed to 2– $\text{SO}_4^{2-}$ .<sup>46</sup> It could be found in Table 3 that the amount of C–O and C=O were higher than D after the addition of  $\text{Fe}_2\text{O}_3$  and the sample DO also exhibited higher –COOH content, testifying that there was a redox reaction between  $\text{Fe}_2\text{O}_3$  and DOA at high temperatures. In addition, based on the fitting result of S 2p, more  $\text{SO}_4^{2-}$  could be detected in DO rather than D, indicating that the S atoms in DOA could be partially oxidized to form S-oxide, which is consistent with the results of TG-MS. The reaction between asphalt molecules and  $\text{Fe}_2\text{O}_3$  could weaken the  $\pi$ – $\pi$  interactions, and the exchange between C, S atoms in DOA and O atoms in  $\text{Fe}_2\text{O}_3$  could further twist and break the intact carbon layer; both factors help increase the proportion of amorphous carbon.

## Electrochemical performance of materials

The electrochemical performance of the obtained materials was evaluated in coin cells with Na-foil as a counter electrode, and the corresponding results are illustrated in Fig. 5. As depicted, the material DO exhibits higher initial discharge/charge capacities and lower initial coulombic efficiencies (ICE) compared with D (43.89% vs. 54.29%) at 0.1C, which is caused by higher BET surface area and more defects. After 3 cycles, sample D only retains 177.2  $\text{mA h g}^{-1}$  discharge capacity, but DO still holds 246.6  $\text{mA h g}^{-1}$ . Due to the lack of stable Na–C intercalation compounds and the larger ionic radius, it is difficult for  $\text{Na}^+$  to enter into the turbostratic lattice of carbon materials. The addition of  $\text{Fe}_2\text{O}_3$  increased the defect degree and the content of amorphous carbon with larger interlayer spacing, which enhanced the capacity of Na-ions. The rate and cyclic performance were measured to further test the sodium storage performance. As shown in Fig. 5c, it could be clearly seen that the sample DO delivers better rate capacity than D at different current densities. Moreover, the capacity of DO returns to 200.1  $\text{mA h g}^{-1}$  with the current density shifted back to 0.1C, while for D, the value is 149.6  $\text{mA h g}^{-1}$ . After the rate capability test, DO also showed great cycling performance, as illustrated in Fig. 5d. During the thermal treatment process, the addition of

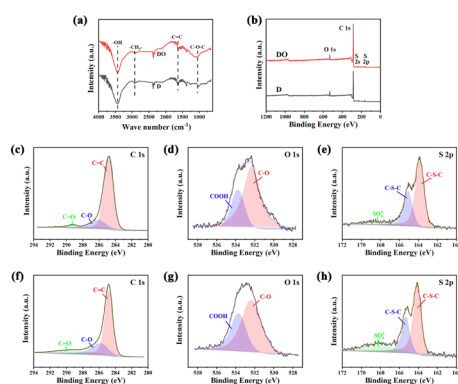


**Fig. 4** FTIR spectra (a); XPS surveys of two samples (b); high-resolution C 1s (c), O 1s (d), and S 2p (e) of sample D; high-resolution C 1s (f), O 1s (g), and S 2p (h) of sample DO.



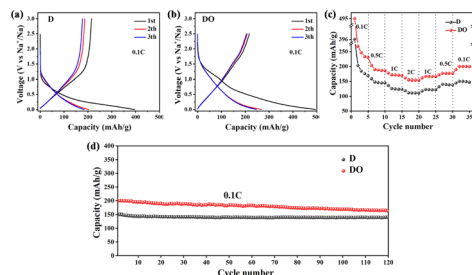


Fig. 5 Charge and discharge profiles of D (a) and DO (b) at 0.1C; rate performance (c) and cycling performance (d) of two samples.

Fe<sub>2</sub>O<sub>3</sub> hindered the formation of PPAMs and weakened the  $\pi$ - $\pi$  interactions between polycyclic aromatic hydrocarbons, resulting in the formation of shorter and disordered carbon nanocrystallites, which enhanced the electrochemical performance of the resulting material. Despite these promising results, the low initial coulombic efficiency caused by the high BET surface area limits the electrochemical applications of DO. In future investigations, it might be possible to decrease the BET surface area by adjusting the size and morphology of Fe<sub>2</sub>O<sub>3</sub> and/or increasing the final calcination temperature.

### The role of iron oxide in retarding graphitization

From the above discussion, it is evident that the linkage method between asphalt molecules is crucial for the final microstructure of the carbon material. Hence, based on these results, Fig. 6 illustrates the role of iron oxide in retarding the graphitization of de-oiled asphaltenes. The asphalt pyrolysis mainly follows the free radical mechanism. Lots of free radicals (C<sup>•</sup> and H<sup>•</sup>) were formed in the initial stage of the high-temperature treatment. Asphalt derived from the solvent deasphalting process holds a high H content due to many long alkyl side chains. Excessive hydrogen free radicals could weaken the reactivity of carbon-free radicals, which is favorable for asphalt molecules to generate the PPAM *via* slow aromatization and polycondensation. With the increasing size, the  $\pi$ - $\pi$  interactions between PPAMs become so strong that the lamellar molecules could orderly stack to form a graphite-like structure. After the addition of Fe<sub>2</sub>O<sub>3</sub>, the hydrogen-free radicals were partially consumed by the oxygen species; meanwhile, the C<sup>•</sup> could polycondense with the Fe<sub>2</sub>O<sub>3</sub> as cores. Both factors could hinder the formation of PPAMs and impede the  $\pi$ - $\pi$  interactions, resulting in the formation of a disordered structure. In the

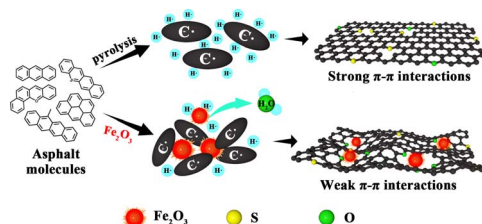


Fig. 6 Schematic diagram of iron oxide in retarding graphitization.

carbonization process, with the temperature increasing over 700 °C, the carbon microcrystalline and the S species could react with Fe<sub>2</sub>O<sub>3</sub>, and O atoms could be embedded into the skeleton to tailor the micro-structure, thus further increasing the content of amorphous carbon. Meanwhile, Fe<sub>2</sub>O<sub>3</sub> could change the morphology of the obtained materials and increase the BET surface area and defects, which enhanced the Na<sup>+</sup> storage sites. Finally, the sample showed better electrochemical performance.

## Conclusions

In summary, this work obtained amorphous carbon from inferior de-oiled asphaltene through direct carbonization of a mixture of DOA and Fe<sub>2</sub>O<sub>3</sub>, and the role of iron oxide in retarding graphitization was studied *via* different characterizations. It was demonstrated that asphalt molecules could polycondense with Fe<sub>2</sub>O<sub>3</sub> as core, and the O species derived from Fe<sub>2</sub>O<sub>3</sub> also could take away the excess H in the initial stage, which inhibited the formation of the planar polycyclic aromatic molecules and weakened the  $\pi$ - $\pi$  interactions, thus increasing the content of the disordered structure. After higher temperature carbonization, the results of TG, FTIR and XPS showed O atoms derived from Fe<sub>2</sub>O<sub>3</sub> could also embed into the carbon skeleton through reaction with DOA, which further twists and breaks the intact carbon layer, thus increasing the proportion of amorphous carbon. Finally, compared with D, the material DO exhibited a higher capability (246.6 vs. 177.2 mA h g<sup>-1</sup> after the third cycle at 0.1C), better rate performance (154.4 vs. 110.9 mA h g<sup>-1</sup> at 2C) and good stability, which could be attributed to higher disorder degree and more defects. Meanwhile, this study provides some important insights into the efficient utilization of residual oil and will promote the development of the solvent deasphalting process.

## Conflicts of interest

There are no conflicts to declare.

## Acknowledgements

The authors gratefully acknowledge financial support by the National Key R&D program of China (No. 2021YFA1501204).

## Notes and references

- 1 W. Han, H. Nie, X. Long and D. Li, *Appl. Catal., A*, 2020, **593**, 117458.
- 2 Y. Gao, W. Han, X. Long, H. Nie and D. Li, *Appl. Catal., B*, 2018, **224**, 330–340.
- 3 Q. Sheng, G. Wang, N. Jin, M. M. Husein and J. Gao, *Fuel*, 2019, **255**, 115736.
- 4 D. Fang, G. Wang, Q. Sheng, S. Ge, C. Gao and J. Gao, *Fuel*, 2019, **257**, 115886.
- 5 J. M. Lee, S. Shin, S. Ahn, J. H. Chun, K. B. Lee, S. Mun, S. G. Jeon, J. G. Na and N. S. Nho, *Fuel Process. Technol.*, 2014, **119**, 204–210.

- 6 N. Jin, G. Wang, S. Han, Y. Meng, C. Xu and J. Gao, *Energy Fuels*, 2016, **30**, 2594–2603.
- 7 L. Zhang, Z. Xu, Q. Shi, X. Sun, N. Zhang, Y. Zhang, K. H. Chung, C. Xu and S. Zhao, *Energy Fuels*, 2012, **26**, 5795–5803.
- 8 Q. Sheng, G. Wang, Q. Zhang, C. Gao, A. Ren, M. Duan and J. Gao, *Energy Fuels*, 2017, **31**, 5037–5045.
- 9 H. Nie, H. Li, Q. Yang and D. Li, *Catal. Today*, 2018, **316**, 13–20.
- 10 N. Li, B. Yan and X.-M. Xiao, *Chem. Eng. Sci.*, 2015, **134**, 230–237.
- 11 T. Zhang, Z. Mao, X. Shi, J. Jin, B. He, R. Wang, Y. Gong and H. Wang, *Energy Environ. Sci.*, 2022, **15**, 158–168.
- 12 H. Liu, Z. Zhu, Q. Yan, S. Yu, X. He, Y. Chen, R. Zhang, L. Ma, T. Liu, M. Li, R. Lin, Y. Chen, Y. Li, X. Xing, Y. Choi, L. Gao, H. S.-y. Cho, K. An, J. Feng, R. Kostecki, K. Amine, T. Wu, J. Lu, H. L. Xin, S. P. Ong and P. Liu, *Nature*, 2020, **585**, 63–67.
- 13 Y. Sun, P. Lu, X. Liang, C. Chen and H. Xiang, *J. Alloys Compd.*, 2019, **786**, 468–474.
- 14 R. Xu, Z. Yi, M. Song, J. Chen, X. Wei, F. Su, L. Dai, G. Sun, F. Yang, L. Xie and C. M. Chen, *Carbon*, 2023, **206**, 94–104.
- 15 N. Yabuuchi, K. Kubota, M. Dahbi and S. Komaba, *Chem. Rev.*, 2014, **114**, 11636–11682.
- 16 C. Huang, J. Yin, W. Shi, Y. Cheng and X. Xu, *Mater. Today Energy*, 2024, **40**, 101501.
- 17 M. Jiang, N. Sun, R. Ali Soomro and B. Xu, *J. Energy Chem.*, 2021, **55**, 34–47.
- 18 Y. Zhao, Y. Cong, H. Ning, X. Fei, C. Wu, H. Wang, Z. He, Y. Wang, Q. Zhao and M. Wu, *J. Alloys Compd.*, 2022, **918**, 165691.
- 19 Y.-E. Zhu, H. Gu, Y.-N. Chen, D. Yang, J. Wei and Z. Zhou, *Ionics*, 2018, **24**, 1075–1081.
- 20 Y. Liu, B. V. Merinov and W. A. Goddard, *Proc. Natl. Acad. Sci. U. S. A.*, 2016, **113**, 3735–3739.
- 21 X. Hu, X. Sun, S. J. Yoo, B. Evanko, F. Fan, S. Cai, C. Zheng, W. Hu and G. D. Stucky, *Nano Energy*, 2019, **56**, 828–839.
- 22 S. Ghosh, V. K. Kumar, S. K. Kumar, U. Sunkari, S. Biswas and S. K. Martha, *Electrochim. Acta*, 2020, **353**, 136566.
- 23 C. Bommier, T. W. Surta, M. Dolgos and X. Ji, *Nano Lett.*, 2015, **15**, 5888–5892.
- 24 Y. Wang, N. Xiao, Z. Wang, H. Li, M. Yu, Y. Tang, M. Hao, C. Liu, Y. Zhou and J. Qiu, *Chem. Eng. J.*, 2018, **342**, 52–60.
- 25 Y. Qi, Y. Lu, L. Liu, X. Qi, F. Ding, H. Li, X. Huang, L. Chen and Y.-S. Hu, *Energy Storage Mater.*, 2020, **26**, 577–584.
- 26 Y. Jiang, J. Jiang, P. Nie, W. Guo, C. Geng, Z. Sun, Y. Fei, Y. Chen, Q. Zhuang, Z. Xing, Z. Ju and H. Shao, *J. Energy Storage*, 2023, **72**, 108484.
- 27 W. S. Du, C. Sun and Q. Sun, *Materials*, 2023, **16**, 4871.
- 28 S. Wei, X. Deng, W. Li, K. Liu, J. Wang, H. Zhao and X. Wang, *Chem. Eng. J.*, 2023, **455**, 140540.
- 29 N. Daher, D. Huo, C. Davoisne, P. Meunier and R. Janot, *ACS Appl. Energy Mater.*, 2020, **3**, 6501–6510.
- 30 M. Xie, X. Zhu, D. Li, Z. Xu, Y. Huang, H. Zha, M. Ding and C. Jia, *J. Power Sources*, 2021, **514**, 230593.
- 31 Q. Sun, D. Li, J. Cheng, L. Dai, J. Guo, Z. Liang and L. Ci, *Carbon*, 2019, **155**, 601–610.
- 32 A. Beda, P.-L. Taberna, P. Simon and C. Matei Ghimbeu, *Carbon*, 2018, **139**, 248–257.
- 33 D. Yu, L. Zhou, J. Tang, J. Li, J. Hu, C. Peng and H. Liu, *Ind. Eng. Chem. Res.*, 2017, **56**, 8880–8887.
- 34 N. Sun, Z. Guan, Y. Liu, Y. Cao, Q. Zhu, H. Liu, Z. Wang, P. Zhang and B. Xu, *Adv. Energy Mater.*, 2019, **9**, 1901351.
- 35 Y. Cao, L. Xiao, M. L. Sushko, W. Wang, B. Schwenzer, J. Xiao, Z. Nie, L. V. Saraf, Z. Yang and J. Liu, *Nano Lett.*, 2012, **12**, 3783–3787.
- 36 J. Niu, R. Shao, J. Liang, M. Dou, Z. Li, Y. Huang and F. Wang, *Nano Energy*, 2017, **36**, 322–330.
- 37 Y. Wang, Z. Wang, Y. Chen, H. Zhang, M. Yousaf, H. Wu, M. Zou, A. Cao and R. P. S. Han, *Adv. Mater.*, 2018, **30**, 1802074.
- 38 B. Xing, C. Zhang, Q. Liu, C. Zhang, G. Huang, H. Guo, J. Cao, Y. Cao, J. Yu and Z. Chen, *J. Alloys Compd.*, 2019, **795**, 91–102.
- 39 S. Huang, H. Guo, X. Li, Z. Wang, L. Gan, J. Wang and W. Xiao, *J. Solid State Electrochem.*, 2013, **17**, 1401–1408.
- 40 P.-Y. Zhao, J.-J. Tang and C.-Y. Wang, *J. Solid State Electrochem.*, 2017, **21**, 555–562.
- 41 M. Yuan, B. Cao, C. Meng, H. Zuo, A. Li, Z. Ma, X. Chen and H. Song, *Chem. Eng. J.*, 2020, **400**, 125948.
- 42 G. Yuan, X. Li, X. Xiong, Z. Dong, A. Westwood, B. Li, C. Ye, G. Ma, Z. Cui, Y. Cong, J. Zhang and Y. Li, *Carbon*, 2017, **115**, 59–76.
- 43 W. Si, J. Zhou, S. Zhang, S. Li, W. Xing and S. Zhuo, *Electrochim. Acta*, 2013, **107**, 397–405.
- 44 J.-Y. Cheng, Z.-L. Yi, Z.-B. Wang, F. Li, N.-N. Gong, A. Ahmad, X.-Q. Guo, G. Song, S.-T. Yuan and C.-M. Chen, *Electrochim. Acta*, 2020, **337**, 135736.
- 45 L. He, Y.-r. Sun, C.-l. Wang, H.-y. Guo, Y.-q. Guo, C. Li and Y. Zhou, *New Carbon Mater.*, 2020, **35**, 420–427.
- 46 Z. Liu, W. Han, D. Hu, H. Nie, Z. Wang, S. Sun, Z. Deng and Q. Yang, *Catal. Sci. Technol.*, 2020, **10**, 5218–5230.

